Carbohydrate Polymers 346 (2024) 122483

Contents lists available at ScienceDirect

Carbohydrate Polymers

journal homepage: www.elsevier.com/locate/carbpol

Molecular modeling study to unravel complexation of daclatasvir and its enantiomer by β-cyclodextrins. Computational analysis using quantum mechanics and molecular dynamics

Paola Peluso [a,*], Roberto Dallocchio [a], Alessandro Dessì [a], Antonio Salgado [b], Bezhan Chankvetadze [c], Gerhard K.E. Scriba [d,*]

[a] Istituto di Chimica Biomolecolare, Consiglio Nazionale delle Ricerche, Traversa La Crucca, 3 - Regione Baldinca - Li Punti, 07100 Sassari, Italy
[b] University of Alcalá, NMR Spectroscopy Centre (CERMN), CAI Químicas, Faculty of Pharmacy, 28805 Alcalá de Henares, Madrid, Spain
[c] Institute of Physical and Analytical Chemistry, School of Exact and Natural Sciences, Tbilisi State University, 0179 Tbilisi, Georgia
[d] Friedrich Schiller University Jena, Department of Pharmaceutical/Medicinal Chemistry, Philosophenweg 14, 07743 Jena, Germany

ARTICLE INFO

Keywords:
Capillary electrophoresis
Cyclodextrin
Enantioseparation
Molecular modeling
Selector-selectand complexation

ABSTRACT

A computational study was performed to unravel mechanisms underlying capillary electrophoresis enantioseparations of daclatasvir and its (*R*,*R*,*R*,*R*)-enantiomer with native and methylated β-cyclodextrins (β-CDs) as chiral selectors. Considering the enantioseparation results as benchmark, the structures of β-CD and seven methylated β-CDs were optimized by quantum mechanics, and their topography and computed molecular properties were compared. Furthermore, the electron charge density distribution of the macrocycles was also evaluated by calculating the molecular electrostatic potential of pivotal regions of native and methylated β-CDs. The function of hydrogen bonds in the complexation process of daclatasvir and the CDs was derived from quantum mechanics analysis and confirmed by molecular dynamics, as orthogonal computational techniques. The presence of a round-shaped cavity in the CDs used as chiral selector appeared as a necessary requirement for the enantioseparation of daclatasvir and its (*R*,*R*,*R*,*R*)-enantiomer. In this regard, it was confirmed that the round shape of the CDs is sustained by hydrogen bonds formed between adjacent glucopyranose units and blocking rotation of the linking glycosidic bonds. The presence of hydroxy groups at the 6-position of the glucopyranose units and the concurrent absence of hydroxy groups at the 2-position were evidenced as important factors for enantioseparation of daclatasvir and its enantiomer by methylated β-CDs.

1. Introduction

Apart from high-performance liquid-chromatography, capillary electrophoresis (CE) has been established as a major technique for analytical enantioseparations (Chankvetadze, 2018; Chankvetadze & Scriba, 2023; El Deeb et al., 2021; Jáč & Scriba, 2013; Krait, Konjaria, & Scriba, 2021). In CE, a chiral selector is added to the background electrolyte, and cyclodextrins (CDs) have been versatile and the most frequently applied chiral selectors (Fejős et al., 2020; Hancu et al., 2021; Peluso & Chankvetadze, 2021; Zhu & Scriba, 2016). CDs are cyclic oligosaccharides composed of α-1,4 linked D-glucopyranose units. The most popular CDs comprise α-CD, β-CD, and γ-CD, which are composed of 6, 7 and 8 glucopyranose units, respectively. The glucopyranose units form a hollow toroid with a lipophilic cavity and a hydrophilic outside. The wider rim contains the secondary 2- and 3-hydroxy functions, while the narrower rim features the primary 6-OH groups. The hydroxy groups can be derivatized resulting in a large variety of uncharged as well as charged derivatives. These comprise so-called single isomer CDs, which possess a defined derivatization pattern, as well as randomly substituted CDs, which are a mixture of substitutional and positional isomers.

Enantioseparations in the presence of CDs are typically mediated by the stereoselective formation of diastereomeric inclusion complexes between a CD and the analyte enantiomers via inclusion of lipophilic moieties of the solutes into the toroidal cavity either from the wider or the narrower side displacing water molecules from the cavity as one of the driving forces of the process (Biedermann et al., 2014; Sandilya et al., 2020). Hydrophobic and van der Waals interactions as well as hydrogen bonds (HBs) are believed to be primarily involved in complex

* Corresponding authors.
E-mail addresses: paola.peluso@cnr.it (P. Peluso), gerhard.scriba@uni-jena.de (G.K.E. Scriba).

https://doi.org/10.1016/j.carbpol.2024.122483
Received 12 April 2024; Received in revised form 8 July 2024; Accepted 9 July 2024
Available online 14 July 2024

formation and stabilization. Steric factors as well as ionic interactions in the case of charged CDs may contribute as well. Furthermore, enantioseparations based solely on the formation of external interactions have been reported. For a summary of chiral recognition mechanisms in CD-mediated analytical enantioseparations see, for example (Chankvetadze & Scriba, 2023; Lämmerhofer, 2010; Scriba, 2016; Scriba, 2019). Several factors impact the enantioseparation of a given chiral analyte at the molecular level, and the stereoselectivity and the enantiomer migration order may depend on the type of the CD, the cavity size, as well as the substituent(s) and substitution pattern of the CDs.

Within time, molecular modeling has become a useful tool to explain experimental processes at the molecular level (Gubbins & Moore, 2010). This is due to the significant improvement of software and hardware available to address issues related to mechanisms and noncovalent interaction functions in chemistry and life sciences (Peluso & Chankvetadze, 2024). Modeling enantioselective recognition processes occurring in liquid-phase separation science remain a challenging issue and the currently available theoretical tools are often inadequate to properly describe the fine mechanisms underlying liquid-phase chromatographic and electromigration processes. This is due to three main reasons (Peluso & Chankvetadze, 2022): (1) the cumulative nature of separation processes such as chromatography and electrophoresis enables detection of intermolecular recognition with very low values of free energy differences between two competitive pathways, (2) the multistep feature of chromatographic and electromigration enantioseparation processes makes it difficult to deconvolute them at molecular level compared to one-step enantioselective processes, and (3) liquid-phase enantioselective recognition involves large solvated molecular systems and most computational methods applied to this field still lack proper validation. Thus, integration of computational and experimental data may help to improve the issue because a mutual exchange of information between experimental and computational analysis may drive essential advancement in enantioseparation science. Indeed, if theoretical and computational analysis are needed to explain experimental processes, benchmark experimental data, in turn, are required to validate theoretical tools and approaches (Peluso et al., 2019; Peluso & Chankvetadze, 2024; Sardella et al., 2020).

CDs and their complexes with various guest molecules have been frequently modelled given that the construction of CD-based virtual models is favoured by the availability of crystallographic structures for several macrocycle derivatives (Chankvetadze & Scriba, 2023; Peluso & Chankvetadze, 2021; Quevedo & Zoppi, 2018). Molecular dynamics (MD) and molecular docking as computational techniques as well as molecular mechanics, semiempirical, and hybrid quantum mechanics (QM) methods for the calculation of optimized structures and related energies are generally used in this field. Density functional theory (DFT) methods were used to model molecular properties of native CDs (Jiménez & Alderete, 2008; Pinjari et al., 2006; Stachowicz et al., 2011), and CD complexes of small/moderate size almost exclusively (Geue et al., 2023; Nowak et al., 2018; Rubim et al., 2024) due to the high computational cost of such methods for large systems. In the last few years, methodological (Henriksen & Gilson, 2017; Sandilya et al., 2020) and applied studies (Khuntawee et al., 2017; Li et al., 2012; Mazurek et al., 2021; Peluso et al., 2023; Peluso & Chankvetadze, 2021; Perez-Miron et al., 2008) also exploited MD simulations to model CDs and related complexes.

Very recently, we focused our interest on the use of methylated β-CDs as chiral selectors in CE. The full set of single isomer methylated β-CDs (Fig. 1) has been synthesized and evaluated as chiral selectors for the CE enantioseparation of basic analytes by Varga and colleagues (Varga et al., 2019). In a subsequent study, we reported the separation of the enantiomers of daclatasvir (DCV, dimethyl *N*,*N*′-([1,1′-biphenyl]-4,4′-diylbis{1H-imidazole-4,2-diyl-[(2*S*)-pyrrolidine-2,1-diyl][(2*S*)-3-methyl-1-oxobutane-1,2-diyl]})dicarbamate, Fig. 1) by this set of CDs (Krait, Salgado, et al., 2021). DCV is an inhibitor of the hepatitis C nonstructural protein 5 A replication complex (Belema et al., 2014). The structure of the drug is a "symmetrical" biphenyl with two identical halves consisting of an imidazole-pyrrolidine-*N*-methoxycarbonyl-valine moiety with two stereogenic centres. The pharmacological active stereoisomer possesses (*S*,*S*,*S*,*S*) configuration, the enantiomer is (*R*,*R*,*R*,*R*)-configured (*RRRR*-DCV, Fig. 1).

In CE separations of DCV and *RRRR*-DCV using a phosphate buffer, pH 2.5, as background electrolyte and native β-CD as well as single isomer methylated β-CDs as chiral selectors, three types of patterns could be observed (Fig. 2) (Krait, Salgado, et al., 2021):

1) An enantioseparation in case of β-CD, *heptakis*(2-*O*-methyl)-β-CD (2-M-β-CD), and *heptakis*(2,6-di-*O*-methyl)-β-CD (2,6-DM-β-CD), with resolution increasing following the order β-CD < < 2,6-DM-β-CD < 2-M-β-CD (Fig. 2A). Reversal of the enantiomer migration order was observed by changing β-CD (DCV > *RRRR*-DCV) to 2,6-DM-β-CD or 2-M-β-CD (*RRRR*-DCV > DCV).
2) A single broad peak in case of *heptakis*(6-*O*-methyl)-β-CD (6-M-β-CD) and *heptakis*(3-*O*-methyl)-β-CD (3-M-β-CD) (Fig. 2B).
3) Two peaks with a plateau for *heptakis*(2,3,6-tri-*O*-methyl)-β-CD (TM-β-CD) and *heptakis*(2,3-di-*O*-methyl)-β-CD (2,3-DM-β-CD) indicating a slow equilibrium (Fig. 2C). The phenomenon of the plateau formation in the case of TM-β-CD had been rationalized by the slow dissociation kinetics of complex using isothermal titration calorimetry and molecular modeling (Peluso et al., 2023).

Heptakis(3,6-di-*O*-methyl)-β-CD (3,6-DM-β-CD) could not be studied in CE due to the extremely low aqueous solubility of this CD (Varga et al., 2019).

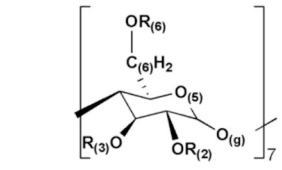

CD	$R_{(2)}$	$R_{(3)}$	$R_{(6)}$
β-CD	H	H	H
2-M-β-CD	CH_3	H	H
3-M-β-CD	H	CH_3	H
6-M-β-CD	H	H	CH_3
2,3-DM-β-CD	CH_3	CH_3	H
2,6-DM-β-CD	CH_3	H	CH_3
3,6-DM-β-CD	H	CH_3	CH_3
TM-β-CD	CH_3	CH_3	CH_3

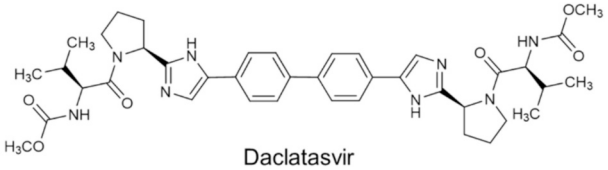

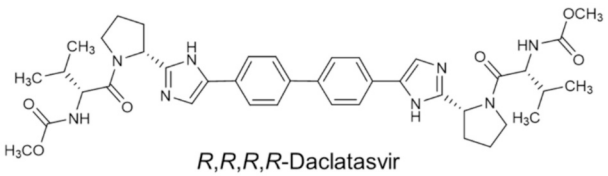

Fig. 1. Structures of daclatasvir, the (*R*,*R*,*R*,*R*)-enantiomer, β-CD and methylated β-CDs. The structures of the CDs are symbolized by the $^4C_1$ chair conformation of the D-glucopyranose residue and numbering/notation of the atoms refers to the description of the respective atoms in the text.

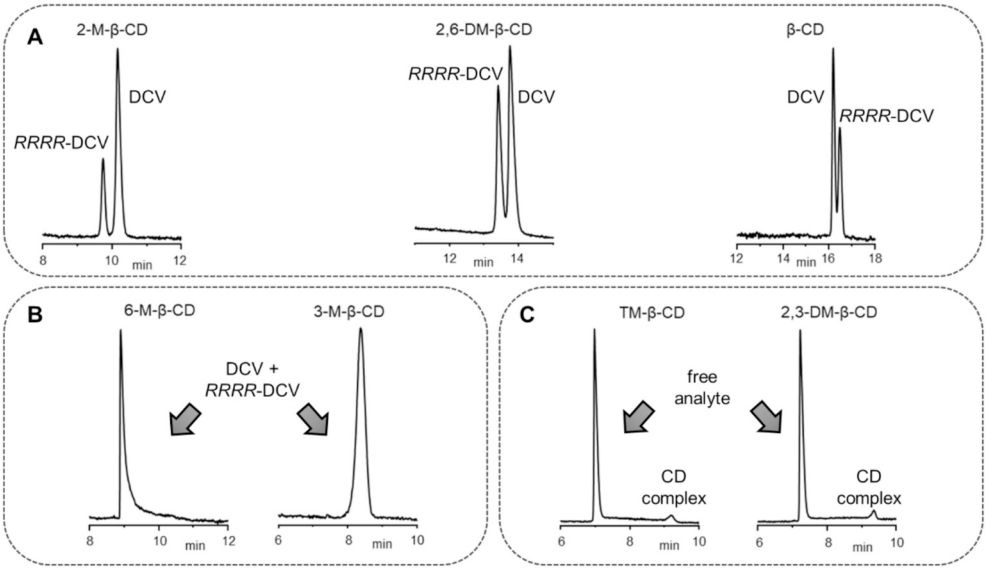

Fig. 2. Electropherograms of the CE separation of a non-racemic mixture of DCV and *RRRR*-DCV (ratio about 2:1) in the presence of the indicated CDs. For experimental details see (Krait, Salgado, et al., 2021).

NMR measurements revealed that 1:1 (DCV:CD) complexes were present in solution in the case of TM-β-CD, 2,3-DM-β-CD and 3-M-β-CD, while higher order complexes with either 1:2 or 1:3 (DCV:CD) stoichiometries were observed for β-CD, 2-M-β-CD, 6-M-β-CD and 2,6-DM-β-CD (Krait, Salgado, et al., 2021). In all cases, the biphenyl moiety was positioned in the cavity of the CDs with the *N*-methoxycarbonyl-valine (MOC-Val) pyrrolidine moieties protruding from both sides of the CD torus. Mass spectrometry data supported the complex stoichiometries concluded from NMR experiments (Krait, Salgado, et al., 2021). Interestingly, as observed for 2,6-DM-β-CD, only a complex with 1:1 stoichiometry was derived from NMR studies when using only a very low CD concentration (unpublished data). Thus, the stoichiometry of the DCV-CD complexes could not explain the behaviour in CE experiments, i.e., enantioseparation versus no separation or plateau formation.

Considering these results as benchmark experimental data, and with the aim of gaining information about the molecular bases of the separations of DCV and *RRRR*-DCV by methylated β-CDs in CE, a molecular modeling study was performed to explore the molecular properties of DCV, β-CDs and their complexes, evaluating their possible impact on the enantioseparations. In this first part, the structures of six methylated β-CDs, namely 2-M-β-CD, 3-M-β-CD, 6-M-β-CD, 2,6-DM-β-CD, 2,3-DM-β-CD, and TM-β-CD were optimized (gas phase) at DFT level using the three-parameter exchange correlation functional due to Becke, Lee, Yang, and Parr (B3LYP) (Becke, 1993). β-CD was included for comparison to get insight into the impact of methylation on the macrocycle structure. Furthermore, the structure of 3,6-DM-β-CD was also optimized for completeness. On this basis, topography and molecular properties were derived by calculations. The electron charge density distribution of the eight β-CDs was also evaluated by calculating the molecular electrostatic potential of certain pivotal regions of the macrocycles mapped on electron density surfaces (V_S) using QM. Accessing V_S could provide information on the strength of the HB sites, i.e. oxygen and hydrogen atoms of the OH groups as HB acceptors and donors, respectively. The function of HBs in the first stages of the inclusion process of DCV and *RRRR*-DCV into the cavities of β-CD, 2-M-β-CD, and 2,6-DM-β-CD was also examined by using MD with explicit water. The hypotheses were (1) whether the methylation at the wider and/or narrow rims of the CD macrocycle could impact intra- and intermolecular HBs, directly or indirectly contributing to DCV-CD binding and recognition and (2) whether these factors could be quantified through molecular modeling using QM and MD as orthogonal computational techniques.

2. Computations

2.1. Quantum mechanics calculations

The 3D structure of β-CD was released from Cambridge Structural Database (CSD) (Thomas et al., 2010), entry AGAZOX (Alexander et al., 2002). The β-CD structure was extracted using the build function, and model kits and tools provided by Spartan '10 Version 1.1.0 (Wavefunction Inc., Irvine, CA, USA) (Shao et al., 2006). Thus, the β-CD model was optimized in the gas phase by using Gaussian 16 W (Wallingford, CT, USA) (Frisch et al., 2016) at DFT level of theory using the B3LYP functional and the 6-31G(d) basis set, applying tight convergence criteria. All methylated β-CDs were built using the DFT optimized CSD β-CD structure as a template and exchanging the proper hydroxy hydrogen atoms bound to the $O_{(2)}n$, $O_{(3)}n$ and/or $O_{(6)}n$ atoms ($1 \leq n \leq 7$) to methyl groups, and optimized at DFT level in the gas phase with the B3LYP functional and 6-31G(d) as basis set. For each structure, vibration frequencies were also calculated to validate the minimization process. Complete computational results and coordinates of the optimized CD structures are reported in the Supporting Information. In Fig. 1, labels and numbering of the atoms of a D-glucopyranose unit in the typical $^4C_1$ chair conformation are shown. Energies are reported in Hartree, dipole moment in Debye and quadrupole moment XX, YY, and ZZ components (Q_{xx}, Q_{yy}, Q_{zz}) in Debye-Å. For all structures, geometric parameters, distances [Å] and angles (°), were measured by using Chimera version 1.16 program (Pettersen et al., 2004). *V* maxima and minima mapped on the molecular electron density isosurfaces ($V_{S,max}$ and $V_{S,min}$) (au, electrons/Bohr) were calculated by using Gaussian 16 W (Frisch et al., 2016). The electrostatic potential in a point **r**, $V(\mathbf{r})$, is given by Eq. (1):

$$V(\mathbf{r}) = \sum_A \frac{Z_A}{R_A - r} - \int \frac{\rho(r)dr'}{|r' - r|} \quad (1)$$

where Z_A is the charge on nucleus A located at R_A, and $\rho(\mathbf{r})$ is the electron density function. The sign of $V(\mathbf{r})$ is positive (the effect of the nuclei is dominant) or negative (the effect of electrons is dominant) on sites acting as HB donors (electrophiles) or acceptors (nucleophiles), respectively. A search for the exact location of $V_{S,max}$ and $V_{S,min}$ was

made through the Multiwfn code (Lu & Chen, 2012a) and through its module enabling quantitative analyses of molecular surfaces (isovalue 0.001 au) (Lu & Chen, 2012b). For all CDs, the area of the electron density isosurface and the volume enclosed by the electron density isosurface were generated by Marching Tetrahedra Algorithm in the Multiwfn code (Lu & Chen, 2012a, 2012b). The .wfn files were obtained through the Gaussian 16 W package.

2.2. Molecular dynamics simulations

For the MD simulations of DCV manually docked in the proximity of β-CD, 2-M-β-CD, and 2,6-DM-β-CD, geometry optimization of all molecules and point charge derivation were achieved by means of the AM1-BCC method (Jakalian et al., 2000), as implemented in the *sqm* program (Walker et al., 2008) contained in the AMBER Tools (Case et al., 2005) distribution. Computation of lowest energy conformations of DCV and its enantiomer were performed at DFT level [B3LYP/6-31G(d)]. 3D structures of DCV and *RRRR*-DCV were treated as fully protonated in accord with the experimental pH of 2.5 in CE experiments. Generalized Amber Force Field (GAFF) and GLYCAM04 (Basma et al., 2001; Kirschner & Woods, 2001a, 2001b) parameter sets (Case et al., 2018) were used for all atoms. Chimera 1.16 (Pettersen et al., 2004) was also employed for visualization of MD trajectories and 3D figure generation. DCV and each β-CD were immersed in a box of TIP3P water molecules that extended 20 Å away from any solute atom. To achieve electroneutrality in the simulated systems, each positive charge of DCV and derivatives in the CD complexes was neutralized by substituting one chloride ion for a water molecule located close to the most positive electrostatic potential region. Running the AMBER *pmemd.cuda* (Salomon-Ferrer et al., 2013) code in parallel on 4 GeForce Nvidia RTX2080 Ti graphics processing units (GPUs), each simulation contained the following stages. Periodic boundary conditions were applied to simulate a continuous system. Upon reorientation of all solute hydrogens and water molecules, a 1000-steps solvent minimization was performed using the steepest descent method with the macrocycle restrained via a force of 40 kcal·mol^{-1}. Then, the system was gradually heated over 0.5 ns to a target temperature with the macrocycle restrained via a force of 40 kcal·mol^{-1}. The solvent underwent a 1000-steps minimization with a restriction of 40 kcal·mol^{-1}. A short 0.2 ns NPT ensemble MD run was performed with a 30 kcal·mol^{-1} restrain, followed by another 10000-steps energy minimization process. Then, another 0.1 NPT ensemble MD run was performed with a force of 20 kcal·mol^{-1}, followed by a 10000-steps minimization with restrictions of 20 kcal·mol^{-1}. Over 60 ps, a re-heating of the system at a constant volume to the target temperature was performed with a restriction of 20 kcal·mol^{-1}. A 20000-step minimization was performed with restrictions of 20 kcal·mol^{-1}. NPT ensemble 2 ns MD was performed, restriction gradually decreasing from 20 kcal·mol^{-1} to the unrestricted system. The Langevin thermostat was used to maintain the simulation temperature. Finally, the production step was carried out under the equilibrium conditions, and the system was subjected to 100 ns MD simulation. The application of SHAKE to all bonds allowed an integration time step of 2 fs to be used. A cut-off distance of 8 Å was used for nonbonded interactions, and the list of nonbonded pairs was updated every 25 steps. Periodic boundary conditions were applied, and electrostatic interactions were represented using the smooth particle mesh Ewald method (Darden et al., 1993) with a grid spacing of 1 Å. The coupling constant for the temperature and pressure baths was 0.2 ps. The resulting set of 2500 structures for each complex was analyzed with the *cpptraj* module (Roe & Cheatham 3rd, 2013) in AMBER to measure relevant distances and angles. For each complex, the total interaction energy was calculated. The reported energies are mean values that were calculated from 2500 × 3 complexes extracted by snapshots taken every 40 ps from the trajectories of three 100 ns MD replicas. The interaction energy (E_{int}) between the analyte enantiomer and CD was calculated based on the energies of the enantiomer-CD complex, CD, and the analyte enantiomer (eq. 2):

$$E_{int} = E_{enantiomer\text{–}CD\ complex} - E_{enantiomer} - E_{CD} \quad (2)$$

3. Results and discussion

3.1. Optimized structures of CDs and the effect of methylation on the enantioseparation

The size, shape and flexibility of the cavity of a CD are essential elements, which contribute to the features of the complexation process (Perez-Miron et al., 2008; Quevedo & Zoppi, 2018). Based on the computed data reported in Tables S1-S31 (Supporting Information), DFT gas phase optimized structures of the methylated β-CDs were compared with the aim to evaluate the impact of methylation on the topography of the macrocycle cavities. β-CD was used as reference for comparison. In this regard, two types of scenarios could be observed (Fig. 3): (a) approximately round cavities for β-CD as well as 2-M-β-CD, 6-M-β-CD and 2,6-DM-β-CD, and (b) elliptically distorted shapes for 3-*O*-methylated derivatives 3-M-β-CD, 2,3-DM-β-CD, 3,6-DM-β-CD, and TM-β-CD.

In agreement with crystallographic and earlier computational studies (Alexander et al., 2002; Pinjari et al., 2006), the DFT calculated structure of β-CD featured a regular shape sustained by inter-residue intramolecular $O_{(3)}$nH···$O_{(2)}$n' HBs (average H···O length = 1.879 ± 0.001 Å, average O-H···O angle = 164.456° ± 0.41) and weaker intra-residue intramolecular $O_{(6)}$nH···$O_{(5)}$n HBs (average H···O length = 2.324 ± 0001 Å, average O-H···O angle = 106.736° ± 0.040) occurring at the wider and the narrower rim, respectively (Fig. 4A) (Peluso & Chankvetadze, 2021; Pinjari et al., 2006).

On this basis, intramolecular HB patterns and geometric parameters of the structures optimized at DFT level of theory for the eight β-CDs were compared to determine the impact of the position(s) of the methyl group(s) on the shape of the macrocycle. The average lengths and angles (with related standard deviations) associated with the intramolecular HBs of the CD macrocycles are reported in Table 1 (native β-CD and CDs methylated in positions 2 and 6) and Table 2 (CDs methylated in position 3). It is worth mentioning that the strength of the intramolecular HBs in CDs is considered to increase as the H···O distance, typically in the range 1.5–2.4 Å, decreases. A second descriptor useful to evaluate the HB strength is the O-H···O angle as a measure of the deviation of the HB directionality from the ideal reference angle of 180°. Thus, the strength of the HB increases as the O-H···O angle tends to the reference value.

Depending on the methylation degree and the position of the methyl group(s), a counterclockwise HB pattern at the secondary rim and a clockwise HB pattern at the primary rim was observed. In β-CD and 2-M-β-CD, the presence of inter-residue $O_{(3)}$nH···$O_{(2)}$n' HBs at the wider rim and of intra-residue $O_{(6)}$nH···$O_{(5)}$n HBs at the primary rim generated a toroidal structure. Methylation of the 2-hydroxy groups increased the flexibility of the macrocycle and, accordingly, in 2-M-β-CD the average length and angle of the HBs at the wider rim increased and decreased (+0.005 Å, −0.206°), respectively, with a higher variability compared to native β-CD. On the contrary, the geometric parameters of the HBs at the narrower rim changed in the opposite direction (−0.024 Å, +0.576°). Thus, the HBs at the narrower rim were slightly stronger compared to native β-CD most likely due to the steric compression effect exerted by the methyl substituents at the wider rim. For 6-M-β-CD and 2,6-DM-β-CD, methylation at the primary rim generates an elongation of the hydrophobic cavity. In terms of HB patterns, for 6-M-β-CD methylation at the narrow rim exerts a compression on the wider rim that, accordingly, showed stronger inter-residue $O_{(3)}$nH···$O_{(2)}$n' HBs (length decrease = −0.011 Å, angle increase = +0.093°) compared to β-CD and 2-M-β-CD. In the case of 2,6-DM-β-CD, the double compression effect due to concurrent methylation at both the wider and narrower rims

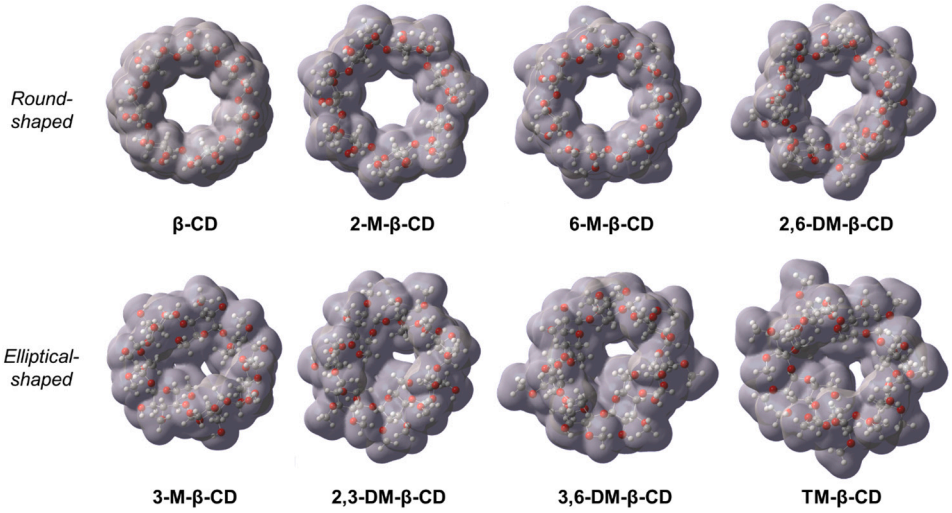

Fig. 3. Electron density isosurfaces (isovalue 0.001 au) of native β-CD and single isomer methylated β-CDs calculated at DFT level of theory [B3LYP/6-31G(d)]. Colour legend: carbon, grey; hydrogen, white; oxygen, red.

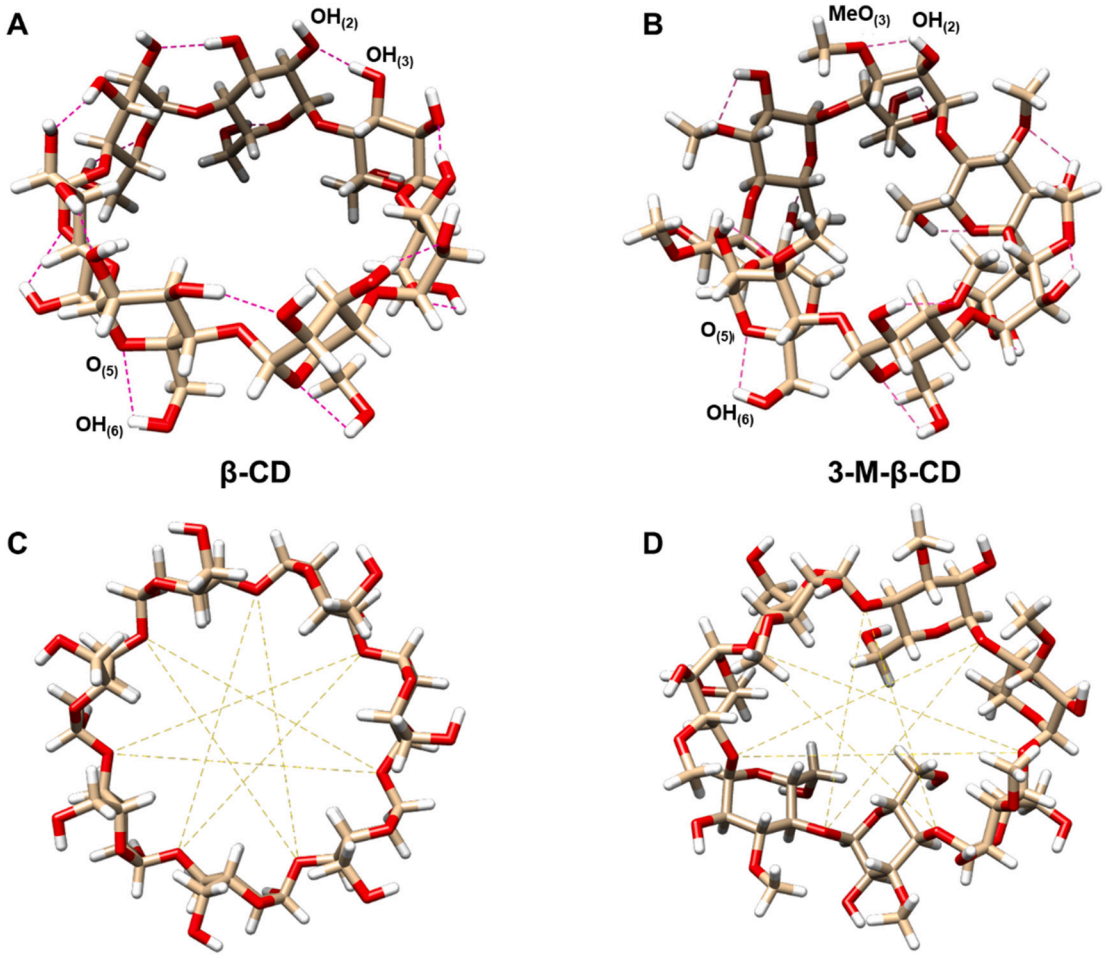

Fig. 4. Comparison of β-CD (A,C) and 3-M-β-CD (B,D) structures: HB pattern (A,B) and schemes of the distance between opposite glycosidic oxygen atoms (C,D). Colour legend: carbon, tan; hydrogen, white; oxygen, red.

increased the disorder degree of the macrocycle and, although the round shape of the CD is preserved, the strength of the HBs decreased (length increase = +0.017 Å, angle decrease = −0.861°).

The elliptically shaped 3-methylated β-CDs showed a different HB pattern at the wider rim. The absence of inter-residue HBs due to the methylation of the 3-hydroxy groups increased the flexibility of adjacent D-glucopyranose units around the glycosidic bonds resulting in a distortion of the regular shape of the macrocycle. In case of 3-M-β-CD and 3,6-DM-β-CD, only weaker intra-residue $O_{(2)}nH\cdots O_{(3)}n$ HBs ($d > 2.2$ Å) could be observed at the wider rim as well as intra-residue

Table 1
Average distances [Å] and angles [°, degree] including the related standard deviations of intramolecular HBs at the wider [inter-residue $O_{(3)}$nH···$O_{(2)}$n'] and at the narrower [intra-residue $O_{(6)}$nH···$O_{(5)}$n] rim, and distance between opposite glycosidic oxygen atoms [$O_{(g)}$n···$O_{(g)}$n'] and between opposite $C_{(6)}$ atoms (narrower rim) [$C_{(6)}$n···$C_{(6)}$n'] ($\Delta R_{l\text{-}s}$) ($1 \leq n \leq 7$), measured for DFT optimized β-CD, 2-M-β-CD, 6-M-β-CD, and 2,6-DM-β-CD structures [B3LYP/6-31G(d)] using the Chimera version 1.16 program.

parameter	β-CD	2-M-β-CD	6-M-β-CD	2,6-DM-β-CD
$O_{(3)}$nH···$O_{(2)}$n' distance	1.879 ± 0.001	1.884 ± 0.0005	1.868 ± 0.003	1.896 ± 0.041
$O_{(3)}$n–H···$O_{(2)}$n' angle	164.46 ± 0.41	164.25 ± 1.22	164.55 ± 0.17	163.60 ± 4.27
$O_{(6)}$nH···$O_{(5)}$n distance	2.324 ± 0.001	2.300 ± 0.008		
$O_{(6)}$n–H···$O_{(5)}$n angle	106.74 ± 0.04	107.32 ± 0.14		
$O_{(g)}$n···$O_{(g)}$n' $\Delta R_{l\text{-}s}$	0.006	0.033	0.025	0.689
$C_{(6)}$n···$C_{(6)}$n' $\Delta R_{l\text{-}s}$	0.013	0.349	0.0183	3.976

Table 2
Average distances [Å] and angles [°, degree] including the related standard deviations of intramolecular HBs at the wider [intra-residue $O_{(2)}$nH···$O_{(3)}$n] and at the narrower [intra-residue $O_{(6)}$nH···$O_{(5)}$n] rim, and distance between opposite glycosidic oxygen atoms [$O_{(g)}$n···$O_{(g)}$n'] and between opposite $C_{(6)}$ atoms (narrower rim) [$C_{(6)}$n···$C_{(6)}$n'] ($\Delta R_{l\text{-}s}$) ($1 \leq n \leq 7$), measured for DFT optimized 3-M-β-CD, 2,3-DM-β-CD, 3,6-DM-β-CD, and TM-β-CD structures [B3LYP/6-31G(d)] using the Chimera version 1.16 program.

parameter	3-M-β-CD	2,3-DM-β-CD	3,6-DM-β-CD	TM-β-CD
$O_{(2)}$nH···$O_{(3)}$n distance	2.209 ± 0.050		2.203 ± 0.052	
$O_{(2)}$n–H···$O_{(3)}$n angle	112.30 ± 1.47		112.50 ± 1.56	
$O_{(6)}$nH···$O_{(5)}$n distance	2.376 ± 0.040	2.368 ± 0.055		
$O_{(6)}$n–H···$O_{(5)}$n angle	105.96 ± 0.65	106.41 ± 1.02		
$O_{(g)}$n···$O_{(g)}$n' $\Delta R_{l\text{-}s}$	2.219	1.948	2.077	1.809
$C_{(6)}$n···$C_{(6)}$n' $\Delta R_{l\text{-}s}$	8.101	8.125	7.997	5.255

$O_{(6)}$nH···$O_{(5)}$n HBs at the narrow rim of the 3-M-β-CD (Fig. 4B). For 2,3-DM-β-CD only weak intra-residue $O_{(6)}$nH···$O_{(5)}$n HBs at the narrow rim could be observed, whereas no HBs could be observed in case of TM-β-CD structure. For this series of 3-methylated β-CDs, the relative strength of the intramolecular HBs appeared to be determined by the relative compression exerted at the wider or the narrower rims depending on the position of the methylation as described for the other methylated CDs above. For the calculated structures of the 3-*O*-methylated derivatives, some -$C_{(6)}H_2$- groups protruding into the macrocycle cavities could be observed at the narrower rim due to the joint effect due to the steric compression exerted by the methylation at the wider rim and the rotation freedom of the glycosyl bonds.

Moreover, in order to monitor the extent of cavity distortion induced by methylation compared to native β-CD, we derived the $\Delta R_{l\text{-}s}$ value as the calculated difference between the longest and the shortest $O_{(g)}$···$O_{(g)}$ and $C_{(6)}$···$C_{(6)}$ distances from the seven pairs of opposing glycosidic oxygen and methylene carbon atoms of the CD (Li et al., 2012). A small value of $\Delta R_{l\text{-}s}$ indicated that the cavity shape was round, whereas a high value revealed an elliptically distorted cavity. The round-shaped CDs showed lower $\Delta R_{l\text{-}s}$ values, ranging from 0.006 to 0.689 Å [$O_{(g)}$···$O_{(g)}$] and from 0.013 to 3.976 Å [$C_{(6)}$···$C_{(6)}$], compared to the elliptic-shaped CDs showing 1.809 Å $\leq \Delta R_{l\text{-}s} \leq$ 2.219 Å and 5.255 Å $\leq \Delta R_{l\text{-}s} \leq$ 8.125 Å for the distances referring to glycosidic oxygen and $C_{(6)}$ atoms, respectively. This resulted in two different distance schemes associated to β-CD and 3-M-β-CD as representative CDs: a regular seven-pointed star (Fig. 4C) in the first case and a distorted seven-pointed star (methylene carbon Fig. 4D) for the methylated macrocycle. For the round-shaped CDs, the $\Delta R_{l\text{-}s}$ values increased following the order β-CD < 6-M-β-CD < 2-M-β-CD < 2,6-DM-β-CD. For the elliptic-shaped macrocycles, the distortion at the wider and the narrower rim followed a different order, i.e. TM-β-CD < 2,3-DM-β-CD < 3,6-DM-β-CD < 3-M-β-CD (wider rim) and TM-β-CD < 3,6-DM-β-CD < 3-M-β-CD < 2,3-DM-β-CD (narrower rim) (see Table 2). These results were consistent with shape and flexibility features observed at the solid state for the crystallographic structures of β-CD (Alexander et al., 2002), 2,6-DM-β-CD (Harata, 1988), and TM-β-CD (Harata et al., 1992).

With the aim to conclude the electron distribution of the β-CD derivatives, the dipole moment, the polarizability α, and the quadrupole moment (*Q*) were extracted from the DFT computed data set [Table 3 (native β-CD and CDs methylated at positions 2 and 6) and Table 4 (CDs methylated at position 3)].

Whereas native β-CD and CDs methylated at both rims, i.e. 2,6-DM-β-CD, 3,6-DM-β-CD and TM-β-CD, showed lower dipole moments ranging from 0.74 to 1.69 Debye irrespective of their shape, higher dipole moments ranging between 3.65 and 5.23 Debye were calculated for CDs methylated at only one of the rims. Polarizability α, providing an estimate of the tendency of distortion of the electron charge distribution in the presence of an external electric field, was shown to increase as the methylation degree also increased. Thus, β-CD and TM-β-CD featured the lowest (549.32 au) and the highest (781.36 au) value of polarizability, whereas *heptakis*(mono)-, and *heptakis*(di)-methylated β-CDs showed intermediate values ranging from 623.28 to 632.12 au and from 701.34 to 709.70 au, respectively. The quadrupole moment is the second order term in the expansion of the total electron distribution, which provides further insight into the overall electron distribution shape of the CDs. For instance, if the XX, YY, and ZZ components of the quadrupole moment are equal, this indicates a spherical electron distribution. Otherwise, as one of these components is larger compared to the others, a distortion due to the elongation of the electron distribution along that axis is revealed. Whereas lower standard deviations could be determined for the *Q* component values along the XX, YY, and ZZ axes in case of the round CDs ranging from ±2.77 to ±7.20 Debye-Å, higher deviations

Table 3
Dipole moments [Debye], polarizability (α) [au], average value of quadrupole moment (*Q*) [Debye-Å], and related standard deviations calculated for DFT optimized structures of β-CD, 2-M-β-CD, 6-M-β-CD, and 2,6-DM-β-CD [B3LYP/6-31G(d)].

parameter	β-CD	2-M-β-CD	6-M-β-CD	2,6-DM-β-CD
Dipole moment	1.69	4.02	3.65	1.03
Polarizability (α)	549.32	632.12	628.86	709.70
Average *Q*	−468.72 ± 2.77	−486.28 ± 7.20	−493.71 ± 4.03	−513.49 ± 3.78

Table 4
Dipole moment [Debye], polarizability (α) [au], average value of quadrupole moment (*Q*) [Debye-Å] (components XX, YY, and ZZ), and related standard deviations calculated for the DFT optimized 3-M-β-CD, 2,3-DM-β-CD, 3,6-DM-β-CD, and TM-β-CD structures [B3LYP/6-31G(d)].

parameter	3-M-β-CD	2,3-DM-β-CD	3,6-DM-β-CD	TM-β-CD
Dipole moment	5.23	4.29	1.14	0.74
Polarizability (α)	623.28	703.82	701.34	781.36
Average *Q*	−502.88 ± 19.25	−522.68 ± 39.05	−535.50 ± 12.91	−556.30 ± 17.68

between the *Q* components were observed for the elliptic 3-M-β-CD, 2,3-DM-β-CD, 3,6-M-β-CD and TM-β-CD ranging between ±12.91 and ± 39.05 Debye-Å.

Correlating geometric features and molecular properties of the methylated β-CDs with the enantioseparation of DCV and its *R*,*R*,*R*,*R*-enantiomer in CE experiments (Fig. 2), it can be concluded that a successful enantioseparation was strictly dependent on the CD cavity shape. A round shape appeared to be a prerequisite for an enantioseparation, although not a guarantee, whereas an elliptic distortion of the CD cavity was detrimental resulting in either no separation (broad peak) or two peaks with a plateau, which did not represent an enantioseparation (Peluso et al., 2023). Within the series of methylated CDs with a round cavity, only 2-M-β-CD and 2,6-DM-β-CD provided enantioseparations of DCV and its enantiomer at a concentration of 8 mM in a sodium phosphate-based BGE, pH 2.5 (Krait, Salgado, et al., 2021). In case of native β-CD, a much higher concentration of 60 mM is required for a partial enantioseparation (Krait, Salgado, et al., 2021). The fact that much lower concentrations of the selectors were required in case of 2-M-β-CD and 2,6-DM-β-CD could be ascribed to the higher flexibility of these two macrocycles compared to 6-M-β-CD or native β-CD. Indeed, 2-M-β-CD and 2,6-DM-β-CD presented weaker HBs at the wider rim, whereas stronger HBs could be observed at the narrower rim for 2-M-β-CD. Furthermore, these two CDs also featured the highest $\Delta R_{l\text{-}s}$ values, confirming superior flexibility and, thus, adaptability to host the chiral guest. In terms of electron charge distribution, it is worth noting that 2-M-β-CD, providing the best enantioresolution under the applied experimental conditions in CE, featured the highest dipole moment compared to β-CD and 6-M-β-CD as well as the highest distortion of the electron charge distribution, as confirmed by the value deviation of the *Q* components (Table S5, Supporting Information). Furthermore, by comparing 2-M-β-CD and 2,6-DM-β-CD remarkable differences in terms of parameters were affected by the electron charge distribution. Thus, to get further insight into this issue, we also calculated and compared the electrostatic potential extrema of pivotal atoms of the macrocycles potentially functioning as HB acceptors [$O_{(g)}$, $O_{(5)}$, $O_{(2)}$, $O_{(3)}$, $O_{(6)}$], featuring negative values of $V_{S,min}$ (nucleophilic sites), and HB donors [$O\underline{H}_{(2)}$, $O\underline{H}_{(3)}$, $O\underline{H}_{(6)}$] featuring positive values of $V_{S,max}$ (electrophilic sites) (Fig. 5). The elliptic-shaped CDs generally showed high electron charge densities on the oxygen atoms compared to the CDs with a round cavity, in particular on $O_{(2)}$ (Fig. 6). This could contribute to slow down the complexation-decomplexation process, which could explain the experimental outcomes of 2,3-DM-β-CD and TM-β-CD (plateau formation) (Peluso et al., 2023) and 3-M-β-CD (broad peak).

However, the most interesting trend could be observed for positive $V_{S,max}$ values describing the electron charge density depletion on hydrogen atoms functioning as HB donors. By changing β-CD to 2-M-β-CD as chiral selector, the hydrogen atom of $OH_{(2)}$ is removed by methylation, which significantly facilitated the enantioseparation. By changing β-CD to 6-M-β-CD, the hydrogen atom of $OH_{(6)}$ is removed by methylation, but in this case, no enantioseparation was observed. Finally, by changing 2-M-β-CD to 2,6-DM-β-CD, the hydrogen atom of $OH_{(6)}$ is removed by methylation, which resulted in a decrease of peak resolution for the enantioseparation. From these data, it could be concluded that (a) the macrocycles functioned as HB donor in the enantiorecognition process, (b) the hydrogen atom of $OH_{(6)}$ was a pivotal site for the enantiorecognition with 2-M-β-CD, while (c) the hydrogen atom of $OH_{(2)}$ exerted a detrimental effect on the enantioseparation using β-CD or 6-M-β-CD.

Given the structure of DCV, pivotal HBs between the analyte and the CDs could occur at two stages of the complexation process. First, at the beginning of the analyte-CD contact, favoring the penetration of the analyte through the wider rim. Second, toward the end of the complexation process, stabilizing the solute-CD complexes through contacts between the folded polar terminal MOC-Val residues of DCV

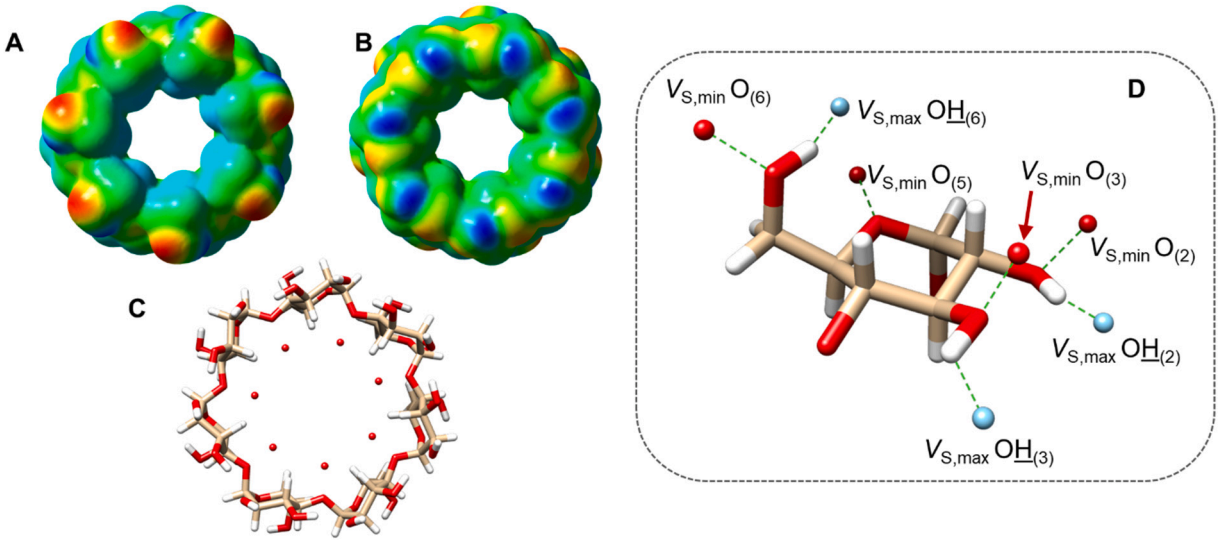

Fig. 5. V_S representations on electron density isosurfaces (0.001 au) of β-CD graphically generated using Gaussian 16 W [DFT/B3LYP/6-31G(d)]: wider rim view (A), narrower rim view (B); colour legend: negative $V_{S,min}$, red; positive $V_{S,max}$, blue; colours in between (orange, yellow, green) depict intermediate V_S values. Location of $V_{S,min}$ calculated for the seven On(g) ($1 \leq n \leq 7$) (C). Location of $V_{S,min}$ and $V_{S,max}$, values calculated on the pivotal regions of each glucopyranose unit of the CDs (D). Colour legend of the tube β-CD structure (C,D): carbon, tan; hydrogen, white; oxygen, red.

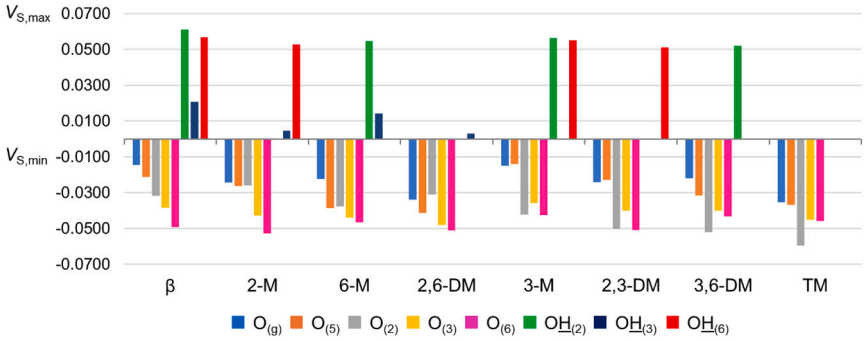

Fig. 6. Average $V_{S,max}$ and $V_{S,min}$ values [au] calculated at DFT level [B3LYP/6-31G(d)] for the $O_{(g)}$, $O_{(5)}$, $O_{(2)}$, $O_{(3)}$, $O_{(6)}$, $O\underline{H}_{(2)}$, $O\underline{H}_{(3)}$, and $O\underline{H}_{(6)}$ atoms of β-CD, 2-M-β-CD, 6-M-β-CD, 2,6-DM-β-CD, 3-M-β-CD, 2,3-DM-β-CD, 3,6-DM-β-CD, and TM-β-CD. For details see Tables S4, S8, S16, S20, S24, S28 and S31 (Supporting Information).

and the CD rim, as confirmed previously by NMR spectroscopy (Krait, Salgado, et al., 2021). With the aim to verify the HB contribution to the complexation process and the enantiorecognition of the analyte by the CDs at the initial stages of the analyte-CD contacts, a series of MD simulations were performed treating solvent explicitly by using the three-site transferrable intermolecular potential (TIP3P) solvation model.

3.2. Molecular dynamics simulations of the first stages of the complexation process

To understand the complexation process and the role of the HBs driving the inclusion of DCV into β-CD, 2-M-β-CD, and 2,6-DM-β-CD, DCV and *RRRR*-DCV were docked outside the CD cavity, and the contacts between analyte and β-CDs were evaluated over 100 ns MD using GLYCAM04 as force field and the three-site TIP3P model to account for solvent explicitly. As previously reported for γ-CD (Peluso et al., 2023), a complete inclusion of the analyte was not observed during this period of time even when increasing the simulation time to 4 microseconds. However, inclusion of the DCV MOC-Val side chain into the CDs was obtained [Table 5, Figs. 7 (β-CD) and 8 (2-M-β-CD)].

MD analysis confirmed that the enantiodifferentiation by the CD cavity originated already at the first stages of the penetration of the enantiomers into the macrocycle cavities through local enantiodifferentiation of the terminal MOC-Val moiety. The enantiomer migration order derived from the interaction energies of the enantiomer-CD complexes extracted from the MD trajectory was consistent with experimental migration order in CE, also accounting for the migration order reversal observed in CE experiments when switching from β-CD (DCV > *RRRR*-DCV) to 2-M-β-CD or 2,6-DM-β-CD (*RRRR*-DCV > DCV). Interestingly, the calculated ΔE_{int} [E_{int} (DCV-CD) - E_{int} (*RRRR*-DCV-CD)] was fully consistent with the experimental enantioresolution (Krait, Salgado, et al., 2021), increasing in the following order β-CD (ΔE_{int} = 0.61 kcal/mol) < 2,6-DM-β-CD (ΔE_{int} = −5.19 kcal/mol) < 2-M-β-CD (ΔE_{int} = −7.52 kcal/mol). In this regard, it is worth mentioning that 7 mM CD concentration was used for the methylated β-CDs (Krait, Salgado, et al., 2021). At this concentration, β-CD showed no ability to enantioseparate DCV and its enantiomer, but a rather high concentration of 60 mM of β-CD was required for a partial enantioseparation. This evidence was fully consistent with the very low ΔE_{int} calculated for β-CD.

In terms of HB pattern, HB lifetime extracted by MD trajectory confirmed that in case of β-CD (Table 5 and Fig. 7) two types of HBs involving the hydrogen atoms of $OH_{(2)}$ and $OH_{(6)}$ as well as the carbonyl groups of the MOC-Val moiety drove the penetration of the analyte into the cavity. Whereas the $OH_{(2)}\cdots O_a = C$ HB showed different lifetimes in

Table 5
Mean interaction energies (E_{int}) and interaction energy difference (ΔE_{int}) of the DCV/β-CD, *RRRR*-DCV/β-CD, DCV/2-M-β-CD, and *RRRR*-DCV/2-M-β-CD complexes, experimental and calculated enantiomer migration order (EMO), and intermolecular C=O···H parameters (lifetime, length, and angle) driving the inclusion of the DCV and *RRRR*-DCV into the CD cavities extracted by MD trajectories. The structure shows the MOC-Val side chain of DCV.

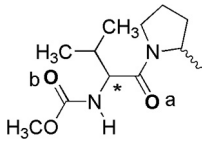

Parameter	DCV/β-CD	*RRRR*-DCV/β-CD	DCV/2-M-β-CD	*RRRR*-DCV/2-M-β-CD
E_{int} [kcal/mol]]	−39.86 ± 8.14	−40.47 ± 8.10	−54.49 ± 7.20	−46.97 ± 8.95
Exp. EMO	DCV > *RRRR*-DCV		*RRRR*-DCV > DCV	
ΔE_{int} [kcal/mol][a]	0.61		−7.52	
Calc. EMO	DCV > *RRRR*-DCV		*RRRR*-DCV > DCV	
$C{=}O_a\cdots H{-}O_{(2)}$				
t [ns]	21.64	43.2		
Length [Å]	2.734	2.758		
Angle [°]	159.79	159.99		
$C{=}O_b\cdots H{-}O_{(6)}$				
t [ns]	27.14	22.84	43.04	32.00
Length [Å]	2.758	2.744	2.741	2.724
Angle [°]	162.03	160.98	163.16	162.18

[a] ΔE_{int} = E_{int} (DCV/CD) - E_{int} (*RRRR*-DCV/CD).

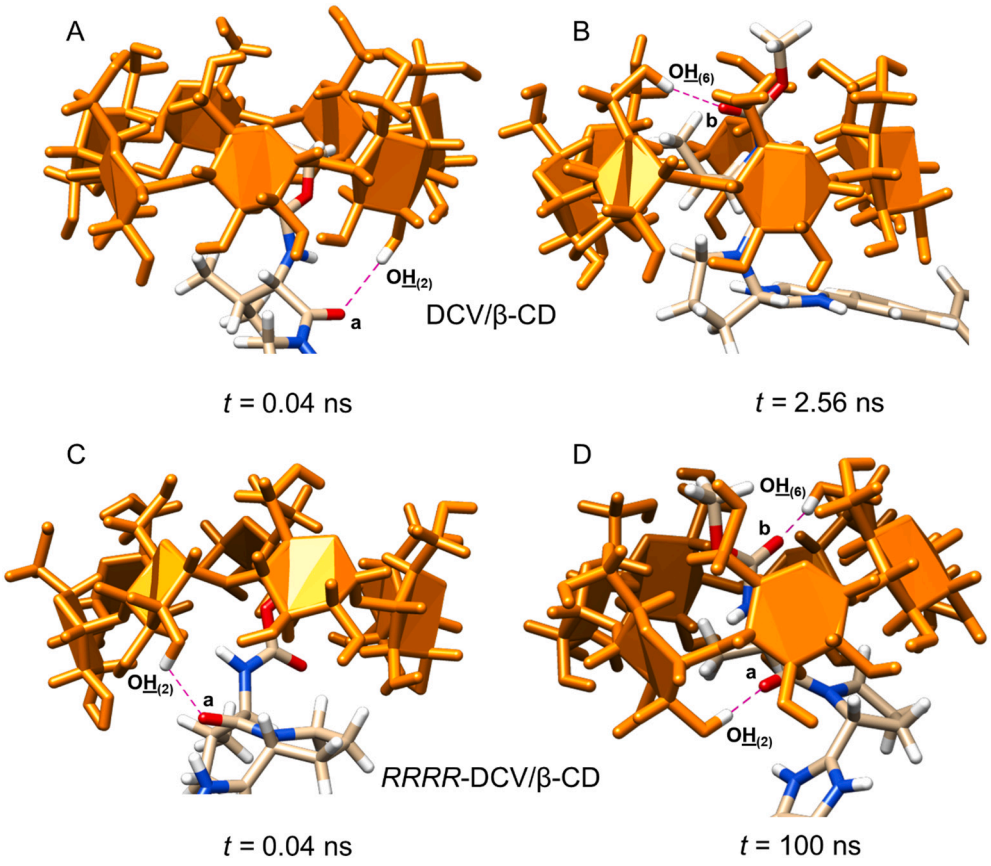

Fig. 7. Representative snapshots of the initial complexation process between DCV and *RRRR*-DCV with β-CD (100 ns MD). The most frequent intermolecular HBs driving the inclusion of the analyte into the CD cavity are indicated as pink dotted lines.

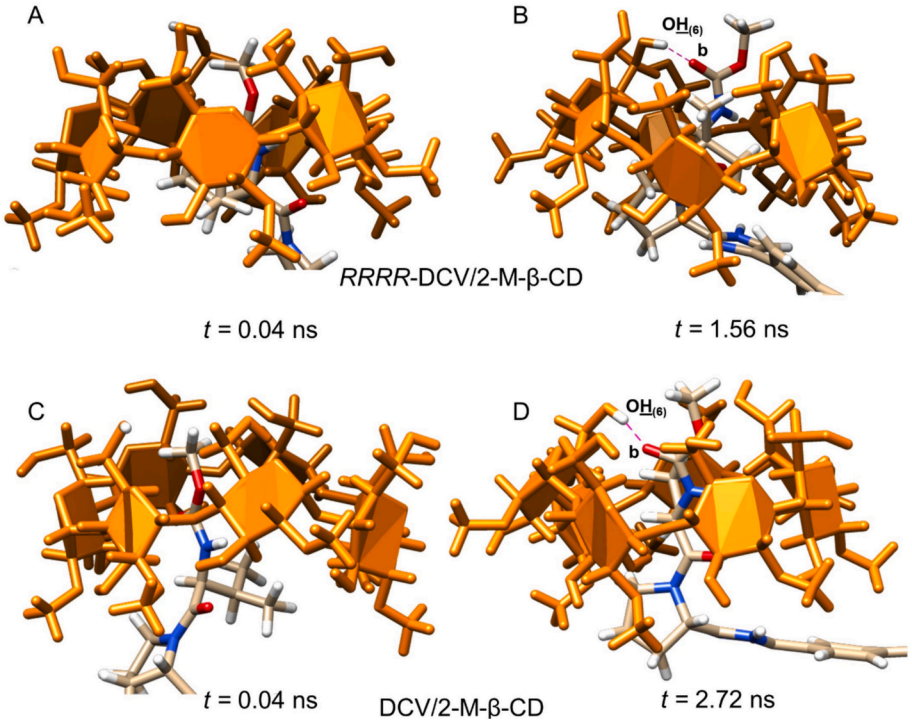

Fig. 8. Representative snapshots of the initial complexation process between DCV and *RRRR*-DCV with 2-M-β-CD (100 ns MD). The most frequent intermolecular HBs driving the inclusion of the analyte into the CD are indicated as pink dotted lines.

the two diastereomeric CD-DCV enantiomer complexes ($\Delta t = 21.56$ ns), the $OH_{(6)}\cdots O_b = C$ HB showed similar lifetimes for both diastereomeric complexes of the DCV enantiomers ($\Delta t = 4.30$ ns). In the case of 2-M-β-CD and 2,6-DM-β-CD, in the absence of the hydrogen atom of $OH_{(2)}$ as HB donor, the initial penetration was driven by hydrophobic forces as shown in the snapshot extracted for the 2-M-β-CD complexes at $t = 0.04$ ns (Fig. 8A and C, data not shown for 2,6-DM-β-CD). Starting from these initial conditions, as shown in the snapshots extracted for the diastereomeric 2-M-β-CD complexes at $t = 1.56$ and 2.72 ns (Fig. 8B and D), the MOC-Val side chain of the analyte directed toward the narrow rim through the formation of HBs with the hydrogen atom of $OH_{(6)}$. For the 2-M-β-CD, the $OH_{(6)}\cdots O_b = C$ HB acted stereoselectively as confirmed by the different lifetimes determined for the two diastereomeric complexes ($\Delta t = 11.04$ ns).

On this basis, the reversal of the enantiomer migration order observed in CE experiments for the methylated β-CDs compared to native β-CD originated from the absence of the hydrogen atom of $OH_{(2)}$ as HB donor. For β-CD, the enantioseparation is stereoselectively controlled by HBs involving the hydrogen atom of $OH_{(2)}$ at the wider rim, whereas in case of 2-M-β-CD the HBs involving the hydrogen atom of $OH_{(6)}$ at the narrow rim contributed to the enantiorecognition. In this context, it is worth noting that 2,6-DM-β-CD enantioseparated DCV and its enantiomer with the same elution order as 2-M-β-CD. Given the fact that 2,6-DM-β-CD cannot form HBs by the hydrogen atom of $OH_{(6)}$, hydrophobic and repulsive forces involving the methyl groups contributed to enantiorecognition as it is also the case for 2-M-β-CD. However, the hydrogen atom of $OH_{(6)}$ of 2-M-β-CD exerted a pivotal role favoring the stereoselective penetration of the analyte into the cavity of this CD, improving enantiorecognition compared to 2,6-DM-β-CD.

4. Conclusions

The CE enantioseparation of DCV and its (*R,R,R,R)*-enantiomer in the presence of native β-CD and single isomer methylated β-CDs as chiral selectors (Krait, Salgado, et al., 2021), raised several issues about the mechanisms and noncovalent interactions underlying solute complexation and enantiorecognition by the CDs. In the frame of a comprehensive project aiming at understanding the molecular bases of these enantioseparations, and at defining a computational protocol suitable to study CD-based enantioseparations at the molecular level, the molecular properties of native and methylated β-CDs and some related complexes were computed to determine their possible impact on the enantioseparation outcomes in CE. With this aim, we explored the impact of the position of the methyl groups and the methylation degree on the shape of the CDs by evaluating the topography, the molecular properties, and the electrostatic potential of seven methylated β-CD structures optimized at the DFT level of theory. Based on the resulting data, the following conclusions could be drawn:

1. All CDs providing enantioseparation of DCV and its enantiomer (β-CD, 2-M-β-CD and 2,6-DM-β-CD) featured a regular round cavity sustained by a counterclockwise set of seven inter-residue $O_{(3)}nH\cdots O_{(2)}n'$ HBs ($1 \leq n \leq 7$). A clockwise set of seven weaker intra-residue $O_{(6)}nH\cdots O_{(5)}n$ HBs could be also observed for β-CD and 2-M-β-CD.
2. CDs containing methyl groups in position 3 and no methyl substituent in position 2 (3-M-β-CD and 3,6-DM-β-CD) featured a counterclockwise set of seven intra-residue $O_{(2)}nH\cdots O_{(3)}n$ HBs. A clockwise set of seven weaker intra-residue $O_{(6)}nH\cdots O_{(5)}n$ HBs were observed for 3-M-β-CD as well as 2,3-DM-β-CD, the latter containing methyl groups in positions 2 and 3. These CDs as well as TM-β-CD exhibited an elliptic cavity and a certain degree of disorder due to free rotation around the α-glycosidic bonds.
3. All elliptic CDs were unable to enantioseparate DCV and its enantiomer providing a single broad peak (3-M-β-CD) or two peaks with a plateau (2,3-DM-β-CD and TM-β-CD). The plateau phenomenon is most likely due to a slow kinetic of the complexation-decomplexation process generated by the steric hindrance exerted by the methyl groups constraining the analyte within the macrocycle cavity and slowing decomplexation (Peluso et al., 2023).

MD simulations of the first stages of the inclusion of the DCV enantiomers into the macrocycle cavities of β-CD, 2-M-β-CD, and 2,6-DM-β-CD provided interaction energies in agreement with the experimental enantiomer migration order. This evidenced that the differentiation between DCV and its enantiomer occurred even in the beginning of the inclusion process with the enantiodifferentiation of the chiral terminal MOC-Val moiety of the analyte. The subsequent use of orthogonal computational techniques like QM and MD simulations allowed to highlight the pivotal role of the hydrogen atom of $OH_{(6)}$ in the enantioseparation and, in parallel, the detrimental function of the hydrogen atom of $OH_{(2)}$. This finding could justify the lack of enantiodifferentiation ability observed for 6-M-β-CD, the higher performance of 2-M-β-CD compared to native β-CD and the lower ability of 2,6-DM-β-CD compared to 2-M-β-CD, as chiral selector toward DCV and its enantiomer.

Confirming the initial hypotheses, the parallel use of QM and MD as orthogonal computational techniques confirmed that the methylation at the wider and/or narrow rims of the CD macrocycles impact intra- and intermolecular HBs contributing to DCV-CD binding and recognition. Methylation of the hydroxy groups of CDs determined the presence and/or the absence of HBs at the wider and at the narrower rims. Also, depending on the position of the non-derivatized hydroxy groups, HBs can be formed between subsequent glucopyranose units blocking rotation of the glycosidic bonds and stabilizing round-shaped CDs. This appears to be a necessary requirement for the enantioseparation of DCV and its *RRRR*-enantiomer in CE. A second requirement for an enantioseparation is the presence of hydrogen atoms of $OH_{(6)}$ determining enantiorecognition, and the concurrent absence of hydrogen atoms of $OH_{(2)}$ favoring binding but slowing the complexation of the analyte by CD. In this regard, it is interesting to note the detrimental effect exerted by the simultaneous presence of hydrogen atoms of $OH_{(2)}$ and absence of the hydrogen atoms of $OH_{(6)}$ on the enantiorecognition capability of 6-M-β-CD. Although 3-M-β-CD and 6-M-β-CD showed similar outcomes in CE experiments (broad peak), for the 3-methylated CD the elliptic shape of the CD cavity and the penetration of some methyl group into the cavity are the major factors limiting the enantiorecognition capability of this CD.

Furthermore, this study reports, to our knowledge, the first comparative structural analysis of the complete series of methylated β-CDs performed through QM. For each CD, cartesian coordinates of the structures optimized at DFT level, under tight convergence criteria, are reported in the Supporting Information.

Finally, the conclusions of this study confirmed that the integration of computational and experimental data is always advisable to avoid computational results which are within the boundaries of theoretical hypotheses but lack experimental confirmation.

CRediT authorship contribution statement

Paola Peluso: Writing – review & editing, Writing – original draft, Methodology, Funding acquisition, Formal analysis, Conceptualization. **Roberto Dallocchio:** Formal analysis, Data curation. **Alessandro Dessì:** Formal analysis, Data curation. **Antonio Salgado:** Writing – review & editing, Data curation. **Bezhan Chankvetadze:** Writing – review & editing, Conceptualization. **Gerhard K.E. Scriba:** Writing – review & editing, Writing – original draft, Conceptualization.

Declaration of competing interest

The authors declare that they have no known competing financial interests or personal relationships that could have appeared to influence the work reported in this paper.

Data availability statement

The data that support the findings of this study are available from the corresponding author upon reasonable request.

Acknowledgements

The authors thank Consiglio Nazionale delle Ricerche (CNR), Italy (Grant no.: SAC.AD002.011.032). Open Access funding provided by Consiglio Nazionale delle Ricerche (CNR) within the CRUI-CARE agreement.

Appendix A. Supplementary data

Supporting information file: Modeling of native β-CD and methylated derivatives: Quantum mechanics data & coordinates. Molecular dynamics: additional data. Supplementary data to this article can be found online at https://doi.org/10.1016/j.carbpol.2024.122483.

References

Alexander, J. M., Clark, J. L., Brett, T. J., & Stezowski, J. J. (2002). Chiral discrimination in cyclodextrin complexes of amino acid derivatives: β-cyclodextrin/N-acetyl-L-phenylalanine and N-acetyl-D-phenylalanine complexes. *Proceedings of the National Academy of Sciences (PNAS), 99*, 5115–5120. https://doi.org/10.1073/pnas.07264759

Basma, M., Sundara, S., Calgan, D., Venali, T., & Woods, R. J. (2001). Solvated ensemble averaging in the calculation of partial atomic charges. *Journal of Computational Chemistry, 22*, 1125–1137. https://doi.org/10.1002/jcc.1072

Becke, A. D. (1993). Density-functional thermochemistry. III. The role of exact exchange. *The Journal of Chemical Physics, 98*, 5648–5652. https://doi.org/10.1063/1.464913

Belema, M., van Nguyen, N., Bachand, C., Deon, D. H., Goodrich, J. T., James, C. A., & … Hamann, L. G.. (2014). Hepatitis C virus NS5A replication complex inhibitors: The discovery of daclatasvir. *Journal of Medicinal Chemistry, 57*, 2013–2032. https://doi.org/10.1021/jm401836p

Biedermann, F., Nau, W. M., & Schneider, H.-J. (2014). The hydrophobic effect revisited – Studies with supramolecular complexes imply high-energy water as a noncovalent driving force. *Angewandte Chemie International Edition, 52*, 11158–11171. https://doi.org/10.1002/anie.201310958

Case, C. A., Ben-Shalom, I. Y., Brozell, S. R., Cerutti, D. S., Cheatham, T. E., III, Cruzeiro, V. W. D., & Kollman, P. A. (2018). *Amber 2018*. San Francisco: University of California.

Case, D. A., Cheatham, T. E., 3rd, Darden, T., Gohlke, H., Luo, R., Merz, K. M., Jr., … Woods, R. J. (2005). The AMBER biomolecular simulation programs. *Journal of Computational Chemistry, 26*, 1668–1688. https://doi.org/10.1002/jcc.20290

Chankvetadze, B. (2018). Contemporary theory of enantioseparations in capillary electrophoresis. *Journal of Chromatography A, 1567*, 2–25. https://doi.org/10.1016/j.chroma.2018.07.041

Chankvetadze, B., & Scriba, G. K. E. (2023). Cyclodextrins as chiral selectors in capillary electrophoresis: Recent trends in mechanistic studies. *Trends in Analytical Chemistry, 160*, Article 116987. https://doi.org/10.1016/j.trac.2023.116987

Darden, T., York, D., & Pedersen, L. (1993). Particle mesh ewald: Anan N·log(N) method for ewald sums in large systems. *Journal of Chemical Physics, 98*, 10089–10092. https://doi.org/10.1063/1.464397

El Deeb, S., Fonseca Silva, C., Jr, S. N., & C., Hanafi, R. S., & Bastos Borges, K.. (2021). Chiral capillary electrokinetic chromatography: Principle and applications, detection and identification, design of experiment, and exploration of chiral recognition using molecular modeling. *Molecules, 26*, 2841. https://doi.org/10.3390/molecules26102841

Fejős, I., Kalydi, E., Malanga, M., Benkovics, G., & Beni, S. (2020). Single isomer cyclodextrins as chiral selectors in capillary electrophoresis. *Journal of Chromatography A, 1627*, Article 461375. https://doi.org/10.1016/j.chroma.2020.461375

Gaussian 16, Revision C.01, Frisch, M. J., Trucks, G. W. Schlegel, H. B. Scuseria, G. E. Robb, M. A. Cheeseman J.R. et al. Gaussian, Inc., Wallingford CT, 2016.

Geue, N., Alcázar, J. J., & Campodónico, P. R. (2023). Influence of β-cyclodextrin methylation on host-guest complex stability: A theoretical study of intra- and intermolecular interactions as well as host dimer formation. *Molecules, 28*, 2625. https://doi.org/10.3390/molecules28062625

Gubbins, K. E., & Moore, J. D. (2010). Molecular modeling of matter: Impact and prospects in engineering. *Industrial & Engineering Chemistry Research, 49*, 3026–3046. https://doi.org/10.1021/ie901909c

Hancu, G., Papp, L. A., Toth, G., & Keleman, H. (2021). The use of dual cyclodextrin chiral selector systems in the enantioseparation of pharmaceuticals by capillary electrophoresis: An overview. *Molecules, 26*, 2261. https://doi.org/10.3390/molecules26082261

Harata, K. (1988). The structure of the cyclodextrin complex. XXI. Crystal structures of heptakis(2,6-di-O-methyl)-β-cyclodextrin complexes with *p*-iodophenol and *p*-nitrophenol. *Bulletin of the Chemical Society of Japan, 61*, 1939–1944. https://doi.org/10.1246/bcsj.61.1939

Harata, K., Hirayama, F., Arima, H., Uekama, K., & Miyaji, T. (1992). Crystal structure of heptakis(2,3,6-tri-O-methyl)-β-cyclodextrin complexes with *m*-iodophenol and 4-biphenylacetic acid. Guest-induced conformational change of a pyranose ring. *Journal of the Chemical Society, Perkin Transactions, 2*, 1159–1166. https://doi.org/10.1039/P29920001159

Henriksen, N. M., & Gilson, M. K. (2017). Evaluating force field performance in thermodynamic calculations of cyclodextrin host−guest binding: Water models, partial charges, and host force field parameters. *Journal of Chemical Theory and Computation, 13*, 4253–4269. https://doi.org/10.1021/acs.jctc.7b00359

Jáč, P., & Scriba, G. K. E. (2013). Recent advances in electrodriven enantioseparations. *Journal of Separation Science, 36*, 52–74. https://doi.org/10.1002/jssc.201200836

Jakalian, A., Bush, B. L., Jack, D. B., & Bayly, I. (2000). Fast, efficient generation of high-quality atomic charges. AM1-BCC model: I. *Method. Journal of Computational Chemistry, 21*, 132–146. https://doi.org/10.1002/(SICI)1096-987X(20000130)21:2<132::AID-JCC5>3.0.CO;2-P

Jiménez, V., & Alderete, J. B. (2008). Hartree-Fock and density functional theory study of α-cyclodextrin conformers. *The Journal of Physical Chemistry A, 112*, 678–685. https://doi.org/10.1021/jp073011o

Khuntawee, W., Karttunend, M., & Wong-ekkabut, J. (2017). Molecular dynamics study of conformations of beta-cyclodextrin and its eight derivatives in four different solvents. *Physical Chemistry Chemical Physics, 19*, 24219–24229. https://doi.org/10.1039/C7CP04009A

Kirschner, K. N., & Woods, R. J. (2001a). Solvent interactions determine carbohydrate conformation. *Proceedings of the National Academy of Sciences (PNAS), 98*, 10541–10545. https://doi.org/10.1073/pnas.191362798

Kirschner, K. N., & Woods, R. J. (2001b). Quantum mechanical study of the nonbonded forces in water-methanol complexes. *Journal of Physical Chemistry A, 105*, 4150–4155. https://doi.org/10.1021/jp004413y

Krait, S., Konjaria, M.-L., & Scriba, G. K. E. (2021). Advances of capillary electrophoresis enantioseparations in pharmaceutical analysis (2017–2020). *Electrophoresis, 42*, 1709–1725. https://doi.org/10.1002/elps.202000359

Krait, S., Salgado, A., Peluso, P., Malanga, M., Sohajda, T., Benkovics, G., … Scriba, G. K. E. (2021). Complexation of daclatasvir by single isomer methylated β-cyclodextrins studied by capillary electrophoresis, NMR spectroscopy and mass spectrometry. *Carbohydrate Polymers, 273*, Article 118486. https://doi.org/10.1016/j.carbpol.2021.118486

Lämmerhofer, M. (2010). Chiral recognition by enantioselective liquid chromatography: Mechanisms and modern chiral stationary phases. *Journal of Chromatography A, 1217*, 814–856. https://doi.org/10.1016/j.chroma.2009.10.022

Li, W.-S., Wang, S.-C., Hwang, T.-S., & Chao, I. (2012). Substituent effect on the structural behavior of modified cyclodextrin: A molecular dynamic study on methylated β-CDs. *Journal of Physical Chemistry B, 116*, 3477–3489. https://doi.org/10.1021/jp207985q

Lu, T., & Chen, F. (2012a). Multiwfn: A multifunctional wavefunction analyser. *Journal of Computational Chemistry, 33*, 580–592. https://doi.org/10.1002/jcc.22885

Lu, T., & Chen, F. (2012b). Quantitative analysis of molecular surface based on improved marching Tetrahedra algorithm. *Journal of Molecular Graphics and Modelling, 38*, 314–323. https://doi.org/10.1016/j.jmgm.2012.07.004

Mazurek, A. H., Szeleszczuk, L., & Gubica, T. (2021). Application of molecular dynamics simulations in the analysis of cyclodextrin complexes. *International Journal of Molecular Sciences, 22*, 9422. https://doi.org/10.3390/ijms22179422

Nowak, P. M., Olesek, K., Woźniakiewicz, M., Mitoraj, M., Sagan, F., & Kościelniak, P. (2018). Cyclodextrin-induced acidity modification of substituted cathinones studied by capillary electrophoresis supported by density functional theory calculations. *Journal of Chromatography A, 1580*, 142–151. https://doi.org/10.1016/j.chroma.2018.10.036

Peluso, P., & Chankvetadze, B. (2021). Native and substituted cyclodextrins as chiral selectors for capillary electrophoresis enantioseparations: Structures, features, application, and molecular modeling. *Electrophoresis, 42*, 1676–1708. https://doi.org/10.1002/elps.202100053

Peluso, P., & Chankvetadze, B. (2022). Recognition in the domain of molecular chirality: From noncovalent interactions to separation of enantiomers. *Chemical Reviews, 122*, 13235–13400. https://doi.org/10.1021/acs.chemrev.1c00846

Peluso, P., & Chankvetadze, B. (2024). Recent developments in molecular modeling tools and applications related to pharmaceutical and biomedical research. *Journal of Pharmaceutical and Biomedical Analysis, 238*, Article 115836. https://doi.org/10.1016/j.jpba.2023.115836

Peluso, P., Dessi, A., Dallocchio, R., Mamane, V., & Cossu, S. (2019). Recent studies of docking and molecular dynamics simulation for liquid-phase enantioseparations. *Electrophoresis, 40*, 1881–1896. https://doi.org/10.1002/elps.201800493

Peluso, P., Landy, D., Nakhle, L., Dallocchio, R., Dessì, A., Krait, S., … Scriba, G. K. E. (2023). Isothermal titration calorimetry and molecular modeling study of the complex formation of daclatasvir by γ-cyclodextrin and trimethyl-β-cyclodextrin. *Carbohydrate Polymers, 313*, Article 120870. https://doi.org/10.1016/j.carbpol.2023.120870

Perez-Miron, J., Jaime, C., & Ivanov, P. M. (2008). Molecular dynamics study on the conformational flexibility and energetics in aqueous solution of methylated β-cyclodextrins. *Chirality, 20*, 1127–1133. https://doi.org/10.1002/chir.20571

Pettersen, E. F., Goddard, T. D., Huang, C. C., Couch, G. S., Greenblatt, D. M., Meng, E. C., & Ferrin, T. E. (2004). UCSF chimera - a visualization system for exploratory research and analysis. *Journal of Computational Chemistry, 25*, 1605–1612. https://doi.org/10.1002/jcc.20084

Pinjari, R. V., Joshi, K. A., & Gejji, S. P. (2006). Molecular electrostatic potentials and hydrogen bonding in α-, β, and γ-cyclodextrins. *The Journal of Physical Chemistry A, 110*, 13073–13080. https://doi.org/10.1021/jp065169z

Quevedo, M. A., & Zoppi, A. (2018). Current trends in molecular modeling methods applied to the study of cyclodextrin complexes. *Journal of Inclusion Phenomena and Macrocyclic Chemistry, 90*, 1–14. https://doi.org/10.1007/s10847-017-0763-z

Roe, D. R., & Cheatham, T. E., 3rd (2013). PTRAJ and CPPTRAJ: Software for processing and analysis of molecular dynamics trajectory data. *Journal of Chemical Theory and Computation, 9*, 3084–3095. https://doi.org/10.1021/ct400341p

Rubim, A. M., Rubenick, J. B., Vendrame, L. O., Zanella, I., Rolim, C. M. B., & Rhoden, C. R. B. (2024). Formulation and characterization of amiodarone-methyl-beta-cyclodextrin inclusion complexes: A molecular modelling perspective. *Journal of Molecular Graphics and Modelling, 126*, Article 108639. https://doi.org/10.1016/j.jmgm.2023.108639

Salomon-Ferrer, R., Götz, A. W., Poole, D., Le Grand, S., & Walker, R. C. (2013). Routine microsecond molecular dynamics simulations with AMBER on GPUs. 2. Explicit solvent particle mesh Ewald. *Journal of Chemical Theory and Computation, 9*, 3878–3888. https://doi.org/10.1021/ct400314y

Sandilya, A., Natarajan, U., & Priya, M. H. (2020). Molecular view into the cyclodextrin cavity: Structure and hydration. *ACS Omega, 5*, 25655–25667. https://doi.org/10.1021/acsomega.0c02760

Sardella, R., Camaioni, E., Macchiarulo, A., Gioiello, A., Marinozzi, M., & Carotti, A. (2020). Computational studies in enantioselective liquid chromatography: Forty years of evolution in docking- and molecular dynamics-based simulations. *Trends in Analytical Chemistry, 122*, Article 115703. https://doi.org/10.1016/j.trac.2019.115703

Scriba, G. K. E. (2016). Chiral recognition in separation science – An update. *Journal of Chromatography A, 1467*, 56–78. https://doi.org/10.1016/j.chroma.2016.05.061

Scriba, G. K. E. (2019). Chiral recognition in separation sciences. Part I: Polysaccharide and cyclodextrin selectors. *Trends in Analytical Chemistry, 120*, Article 115639. https://doi.org/10.1016/j.trac.2019.115639

Shao, A., Molnar, L. F., Jung, Y., Kussmann, J., Ochsenfeld, C., Brown, S. T., … Jr., & Head-Gordon, M.. (2006). Advances in methods and algorithms in a modern quantum chemistry program package. *Physical Chemistry Chemical Physics, 8*, 3172–3191. https://doi.org/10.1039/B517914A

Stachowicz, A., Styrcz, A., Korchowiec, J., Modaressi, A., & Rogalski, M. (2011). DFT studies of cation binding by β-cyclodextrin. *Theoretical Chemistry Accounts, 130*, 939–953. https://doi.org/10.1007/s00214-011-1014-9

Thomas, I. R., Bruno, I. J., Cole, J. C., Macrae, C. F., Pidcok, E., & Wood, P. A. (2010). WebCSD: The online portal to the Cambridge structural database. *Journal of Applied Crystallography, 43*, 362–366. https://doi.org/10.1107/S0021889810000452

Varga, E., Benkovics, G., Darcsi, A., Varnai, B., Sohajda, T., Malanga, M., & Beni, S. (2019). Comparative analysis of the full set of methylated β-cyclodextrins as chiral selectors in capillary electrophoresis. *Electrophoresis, 40*, 2779–2798. https://doi.org/10.1002/elps.201900134

Walker, R. C., Crowley, M. F., & Case, D. A. (2008). The implementation of a fast and accurate QM/MM potential method in AMBER. *Journal of Computational Chemistry, 29*, 1019–1031. https://doi.org/10.1002/jcc.20857

Zhu, Q., & Scriba, G. K. E. (2016). Advances in the use of cyclodextrins as chiral selectors in capillary electromigration techniques – Fundamentals and applications. *Chromatographia, 79*, 1403–1435. https://doi.org/10.1007/s10337-016-3167-0